



Cite this: *New J. Chem.*, 2021, 45, 11831

Bi₂S₃@NH₂-UiO-66-S composites modulated by covalent interfacial reactions boost photodegradation and the oxidative coupling of primary amines†

Hang Wang, Qing Zhang, Qing Liu, Na Zhang,* Jian-Yong Zhang  and Yong-Zheng Fang

Heterojunctions have attracted much attention due to the efficient separation and conduction of charge carriers in the photocatalytic reactions. However, the interfacial energy barrier between two components still limits the controllable assembly, separation, and conduction of photoexcited charge carriers, and further lower the photocatalytic activity. How to control the assembly of the heterojunction and accelerate the separation and conduction of photogenerated electron–holes by building a more intimate interfacial interaction is an important area of research. Herein, we report a series of Bi₂S₃@NH₂-UiO-66-S heterostructures prepared by the covalent interfacial reaction. Novel composites exhibit excellent efficiencies for the photodegradation of methylene blue and the oxidative coupling of benzylamine and its derivatives. The turnover frequency is estimated to be about 8083 μmol g_{cat}⁻¹ h⁻¹. The super photocatalytic performance was attributed to the interfacial compactness by the covalent interfacial reaction. The expansion for the excellent performance was confirmed by UV-vis DRS, photocurrent measurement and EIS.

Received 23rd March 2021,
Accepted 31st May 2021

DOI: 10.1039/d1nj01427g

rsc.li/njc

1. Introduction

In recent years, semiconductor-based photocatalysts have attracted considerable attention in the degradation of organic pollutants, water splitting, CO₂ reduction and organic synthesis under mild conditions because of their low cost, relative safety, and environmental friendliness.^{1,2} Many types of semiconductor materials, such as metal oxide,^{3–5} metal sulfide,^{6–8} and graphitic carbon nitride (g-CN)^{9–11} have been used as photocatalysts in various types of applications.

Among these used photocatalysts, metal organic frameworks (MOFs) constructed from organic linkers and metal clusters are an intriguing class of porous crystalline photocatalysts, owing to their ability to integrate both light-harvesting and catalytic sites in a single solid platform.^{12–15} In 2007, Garcia *et al.* first reported the semiconductor behavior of MOF-5 for the photocatalytic degradation of phenol. Since then, great progress has been achieved in various photocatalytic reactions with the rapid development of MOFs.^{16–21} Despite these successful studies, high efficiency in the utilization of solar energy and conversion based on photoactive MOFs remain scarce considering the poor

electronic conductivity from organic ligands to metal centers in MOFs, particularly for visible-light driven MOF photocatalysts. In order to further enhance the photocatalytic performance, constructing heterojunction semiconductor/MOF photocatalysts has been considered to be an effective method.^{22–24} More importantly, the heterojunction can efficiently disperse semiconductor photocatalysts and offer additional channels for the timely separation of photoexcited charge carriers as a supporting matrix. Furthermore, the created heterojunctions in semiconductor/MOF photocatalysts effectively impede the recombination of photoexcited charge carriers, which contribute markedly to an improved photocatalytic performance. According to these strategies, we recently reported a series of heterojunctions structures, such as Ag₃PO₄@UiO-66, In₂S₃@UiO-66@GO, CdS@NH₂-MIL-125(Ti), Bi₂S₃@ZIF-8(Zn) and In₂S₃@UiO-66. These semiconductor/MOF composites exhibited enhanced photodegradation efficiencies for normal organic dyes and pollutants containing rhodamine (RhB), methyl orange (MO), phenol and oxytetracycline (OTC) under visible-light irradiation compared to pristine materials and normal inorganic photocatalysts.^{25–29} The high photodegradation performance was attributed to the effective heterojunction interface formed in the composites, which suppressed the secondary recombination of photo-generated electron–hole pairs. Nevertheless, the common synthesis route was mainly the epitaxial growth of nanoparticles on the surface of MOFs, and *vice versa*. The interfacial

Shanghai Institute of Technology, Shanghai 201418, P. R. China.

E-mail: nzhang@sit.edu.cn

† Electronic supplementary information (ESI) available. See DOI: 10.1039/d1nj01427g

energy barrier between two components mainly formed from the physical attraction or joining, still causing lower efficiency of separation and conduction of charge carriers in photocatalytic reactions. In order to further control the assembly of the heterojunction and improve the interfacial interaction between MOFs and the semiconductor, post-synthetic modifications (PSMs) were used to functionalize the MOFs, favoring a tight anchoring of the semiconductor nanoparticles.

In this paper, $\text{NH}_2\text{-UiO-66}$ was chosen as the supporting matrix due to the ultrahigh porosity, high thermal and chemical stability, excellent visible-light responsiveness and semiconductor property.^{30,31} In addition, the negatively charged ($-\text{NH}_2$) surface of $\text{NH}_2\text{-UiO-66}$ not only allows metal ions to tightly anchor and wrap, which is beneficial to the rapid fabrication of metal sulfides/ $\text{NH}_2\text{-UiO-66}$ and the creation of an intimate contacted interface in the semiconductor/MOF photocatalysts,^{32–34} but also favors post-synthetic modifications by mercapto acetic acid, which will anchor Bi^{3+} ions as a docking site to enhance the interfacial interactions between UiO-66 and Bi_2S_3 nanoparticles (NPs) (Scheme 1). The resulting $\text{Bi}_2\text{S}_3@/\text{NH}_2\text{-UiO-66-S}$ (termed as $x\text{-BU-S}$, being different from the used $\text{Bi}_2\text{S}_3@/\text{NH}_2\text{-UiO-66}$) heterojunction structures were fabricated through a simple and efficient self-assembly process, which accelerated the photocatalytic reaction under visible light irradiation ($\lambda > 420 \text{ nm}$). Bi_2S_3 NPs are uniformly interspersed on the surface of $\text{NH}_2\text{-UiO-66}$, and the intimate contacted heterojunction interface prevent the recombination of photogenerated charge carriers. The synthesized photocatalysts were characterized by PXRD, SEM, TEM, XPS, BET, UV-Vis DRS, and EIS measurements. The novel composites can be used as heterogeneous photocatalysts to photodegrade methylene blue (MB), and in the oxidative coupling of primary benzylamine and its derivatives into corresponding imines. The enhanced interfacial compactness improves the separation and conduction of the charge carriers in photocatalytic reactions by the covalent interfacial reaction, exploring a new strategy for the fabrication of photocatalytic composites in this work.

2. Experimental

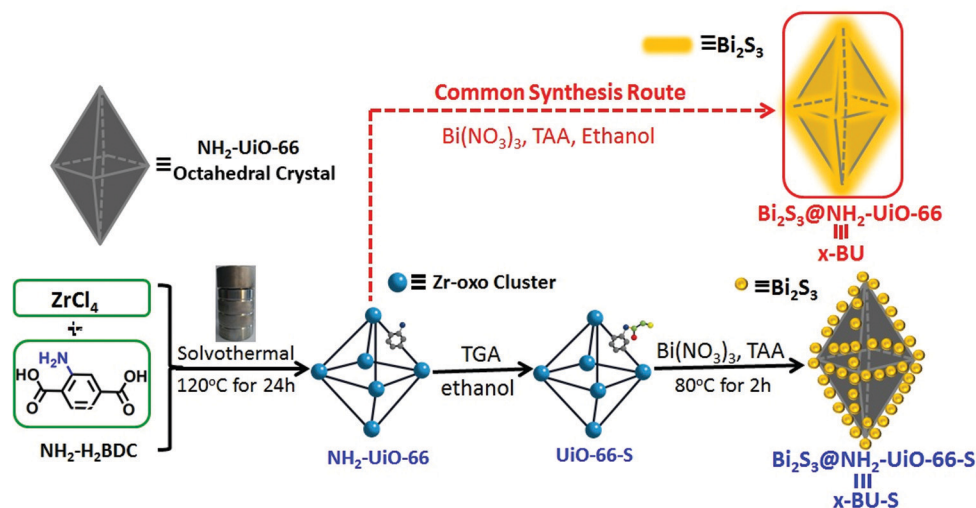
2.1. Materials

Amino terephthalic acid ($\text{NH}_2\text{-BDC}$), zirconium tetrachloride (ZrCl_4), bismuth nitrate pentahydrate ($\text{Bi}(\text{NO}_3)_3 \cdot 5\text{H}_2\text{O}$), thioacetamide ($\text{C}_2\text{H}_5\text{NS}$, TAA), thioglycolic acid ($\text{C}_2\text{H}_4\text{O}_2\text{S}$, TGA), and acetic acid (CH_3COOH) were of analytical grade and used as received without further purification. Distilled water was used throughout the experiment.

2.2. Synthesis

2.2.1 Synthesis of $\text{NH}_2\text{-UiO-66}$. $\text{NH}_2\text{-UiO-66}$ was synthesized according to the literature with some modifications.¹⁸ Briefly, ZrCl_4 (1.0 mmol, 233.0 mg) and $\text{NH}_2\text{-BDC}$ (1.0 mmol, 166.0 mg) were dissolved in the mixed solution consisting of 100 mL N,N -dimethylformamide (DMF) and 6 mL acetic acid, which was added to turn the morphology of $\text{NH}_2\text{-UiO-66}$. The obtained mixture was stirred for 1 h under room temperature, and then sealed in a Teflon-lined autoclave and heated in an oven at 120°C for 24 h. After cooling to room temperature, the solid products were collected by filtration and thoroughly washed by deionized (DI) water and ethanol for three times, and then dried at 60°C in the vacuum drying oven for 12 h.

2.2.2 Synthesis of the $\text{Bi}_2\text{S}_3@/\text{NH}_2\text{-UiO-66-S}$ composite. Different from the previously reported $\text{Bi}_2\text{S}_3@/\text{NH}_2\text{-UiO-66}$ composite (BU), the freshly synthesized $\text{NH}_2\text{-UiO-66}$ was first treated by thioglycolic acid through the covalent interface reactions, forming the mercapto-functionalized $\text{NH}_2\text{-UiO-66}$ pristine (named as UiO-66-S). Typically, 200 mg $\text{NH}_2\text{-UiO-66}$ was dispersed in 40 mL DI water and sonicated for 30 min. The suspension was then transferred into a glass bottle (100 mL) with the addition of 20 mL of thioglycolic acid/ethanol solution (5% volume fraction), and sonicated for 30 min. The UiO-66-S products were collected by filtration and then dried in the vacuum drying oven for 12 h. The obtained UiO-66-S was dissolved in the homogeneous suspension under constant mechanical stirring. Then, 194 mg $\text{Bi}(\text{NO}_3)_3 \cdot 5\text{H}_2\text{O}$ was



Scheme 1 The illustration for the preparation of $\text{Bi}_2\text{S}_3@/\text{NH}_2\text{-UiO-66-S}$ composites.

dissolved in the homogeneous suspension under constant mechanical stirring, followed by the addition of 46 mg TAA. After that, the resultant mixture was stirred and heated at 80 °C with continuous stirring for 2 h. The black products were collected and washed with deionized water and ethanol for several times, and finally dried overnight at 60 °C.

Furthermore, the products with different proportions were referred as *x*-BU-S, where *x* is the mass ratio of Bi₂S₃ to NH₂-UiO-66 (*x* = 0.8, 1.2, and 1.8). For comparison, the Bi₂S₃@NH₂-UiO-66 samples (*x*-BU) were synthesized under the same conditions depicted without thioglycolic acid. Similarly, Bi₂S₃ NPs were synthesized under the same conditions depicted above without NH₂-UiO-66.

2.3. Characterization

Powder X-ray diffraction (PXRD) patterns were collected on a Bruker D8 Advance X-ray diffractometer with CuK α radiation in the 2 θ range of 5–50° (λ = 1.5418 Å, 40 kV, 40 mA). N₂ isothermal adsorption experiments were conducted on a micromeritics surface area analyzer (ASAP-2020) at 77 K. Scanning electron microscopy (SEM) was performed on a S-4800 II microscope (Hitachi). Transmission electron microscopy (TEM) and high-resolution transmission electron microscopy (HRTEM) were conducted on a FEI JEM-2100. UV-Vis diffuse reflectance spectra were obtained on an Agilent Cary 5000 spectrophotometer over a range of 200–800 nm using BaSO₄ as the reflectance standard. X-ray photoelectron spectroscopy (XPS) was performed on a Physical Electronics PHI-5702 system with a monochromatic AlK α source and a charge neutralizer. Electron-spin-resonance (ESR) spectra were recorded on a Bruker ESP 300 E electron paramagnetic resonance spectrometer at room temperature with the signals of the radicals trapped by 5,5-dimethyl-1-pyrroline N-oxide (DMPO).

2.4. Photocatalytic degradation experiments

The photocatalytic degradation of methylene blue was performed to investigate the photocatalytic performance of the as-prepared hybrid photocatalyst samples under visible-light irradiation. In a typical process, 20 mg of photocatalyst was well dispersed in 100 mL of MB solution (10 mg L⁻¹) in a condensation beaker, and the as-obtained suspension was then irradiated under a 300 W xenon lamp fitted with a 420 nm cutoff filter at a separation distance of 20 cm. Prior to irradiation, the suspension was stirred under dark conditions for 45 min to reach an adsorption-desorption equilibrium. During the photodegradation process, stirring was maintained to keep the mixture as a suspension. About 4 mL of the supernatant was then removed from the vessel at different time intervals, and centrifuged to monitor the reaction process using UV-Vis spectroscopy at 665 nm.

2.5. Electrochemical properties test

For investigation of the electrochemical and photoelectrochemical behavior of the as-prepared samples, a standard three-electrode system with Ag/AgCl, Pt foil and the samples coated on FTO glass electrode were used as a standard electrode, a counter electrode, and a working electrode, respectively. The transient photocurrent

response curves were recorded using a CHI instruments electrochemical workstation (model 660D) in a 0.1 M Na₂SO₄ solution under visible-light irradiation. A 500 W xenon lamp with a high-pass filter (420 nm) was used as the light source, and placed 25 cm away from the system. The working electrodes were fabricated according to the following steps: the as-synthesized powders were adhered to a 10 × 10 mm FTO glass *via* Nafion coating, and 10 mg of the powders was dispersed ultrasonically into a 1 wt% Nafion-ethanol solution. Then, the abovementioned homogeneous mixtures were added onto the FTO glass, and the powders attached to the FTO glass could be used as the working electrode after the evaporation of ethanol. Moreover, electrochemical impedance spectroscopy (EIS) tests were carried out at an open circuit potential over the frequency range between 10⁵ and 10⁻¹ Hz.

2.6. General procedure for the benzylamine oxidation-coupling reaction

The photocatalytic oxidative coupling reaction of amines was performed at room temperature. The typical procedure was as follows: a mixture of benzylamine (0.5 mmol), acetonitrile (MeCN, 5 mL), 1.2-BU-S catalyst (10 mg) and *n*-dodecane (100 μ L as the internal standard) was stirred in a 10 mL quartz tube. Under air atmosphere, the reaction was irradiated with a Xe lamp (500 W distance app. 10 cm) with a cutoff filter to remove the ultraviolet light (λ < 420 nm) under an ice bath. After the reaction, the photocatalyst was removed by centrifugation, and the supernatant was monitored by gas chromatography–mass spectrometer (GC-MS, SHIMADZU-QP2010). The temperature program for GC-MS analysis was set as follows: the temperature was held at 40 °C for 1 min, then raised to 280 °C at the rate of 30 °C min⁻¹, and held for 5 min. The inlet and detector temperatures were 280 °C. The analysis was carried out directly after sampling to avoid any additional conversion. In order to carry out the catalyst recycling experiments, the catalyst was recovered by centrifugation and washed with H₂O and ethanol for 3 times, and then dried in air for the following catalysis. The turnover frequency (TOF) values were calculated as the moles of products divided by the mass of the photocatalyst and the reaction time.

3. Results and discussion

3.1. Characterization

The detailed morphology and microstructure of the as-synthesized *x*-BU-S composites were characterized by PXRD, FT-IR, SEM, HRTEM and EDX elemental mapping. First, the PXRD patterns confirmed the successful fabrication of NH₂-UiO-66, Bi₂S₃ and *x*-BU-S. As shown in Fig. 1, the diffraction peaks at 22.3°, 25.0°, 28.6° and 31.7° were indexed to the (2 2 0), (1 3 0), (2 1 1), and (2 2 1) crystal planes of Bi₂S₃ (JCPDS no. 17-0320), respectively.³⁵ The characteristic diffraction peaks at 7.44°, 8.58°, and 25.80° corresponded to the (1 1 1), (0 0 2), and (0 0 6) planes of NH₂-UiO-66, respectively. In the meantime, the narrow diffraction peaks of NH₂-UiO-66 indicate the high crystallinity and fit well with pure UiO-66.^{36,37} This means that

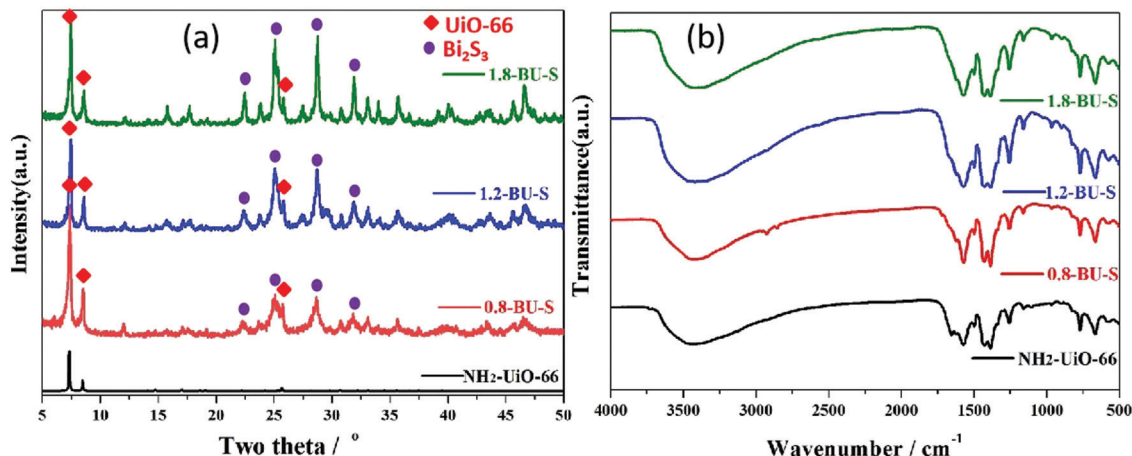


Fig. 1 The PXRD profiles (a) and FT-IR spectra (b) of the synthesized samples.

the framework of $\text{NH}_2\text{-UiO-66}$ remained unchanged after the post-synthetic modifications with thioglycolic acid. As for $x\text{-BU-S}$, characteristic peaks of $\text{NH}_2\text{-UiO-66}$ and Bi_2S_3 could be observed, demonstrating that the Bi_2S_3 samples were successfully crystallized on the surface of $\text{NH}_2\text{-UiO-66}$. On the other hand, the peak intensities of $\text{NH}_2\text{-UiO-66}$ gradually decreased and the peaks of Bi_2S_3 increased with the increasing ratio of Bi_2S_3 . Meanwhile, no obvious shift and excess peaks were detected, indicating that $\text{NH}_2\text{-UiO-66}$ maintained its crystalline structure after Bi_2S_3 deposition. The FT-IR spectra of the samples are shown in Fig. 1b, which are in accordance with the literature.¹⁸ The absorption peaks at 3419 cm^{-1} and 1573 cm^{-1} are assigned to the amino $\nu_{\text{N-H}}$ and carbonyl $\nu_{\text{C=O}}$, respectively. The absorption bands at around 1343 cm^{-1} and 1257 cm^{-1} correspond to the C-N stretching vibration modes. The absorption bands between 765 cm^{-1} and 573.8 cm^{-1} are assigned to the Zr-O modes. The absorption peak at 1566 cm^{-1} is ascribed to the $\nu_{\text{C=C}}$ skeletal vibration of the benzene ring in $\text{NH}_2\text{-UiO-66}$. Moreover, no significant differences were observed between $x\text{-BU-S}$ and $\text{NH}_2\text{-UiO-66}$, confirming the existence of $\text{NH}_2\text{-UiO-66}$ in the composites. The morphological characteristics of all prepared samples are revealed in Fig. 2. From Fig. 2a, the pristine $\text{NH}_2\text{-UiO-66}$ is highly uniform with an octahedral morphology and an average particle size of 200 nm. As a comparison, the pristine Bi_2S_3 tended to aggregate into larger nanospheres, as shown in Fig. 2b. For the 1.2-BU-S composites with various contents of Bi_2S_3 (Fig. 2c and d), it was noticed that the surface of $\text{NH}_2\text{-UiO-66}$ became rough and the octahedral feature was maintained after the modification. The high magnification SEM image in Fig. 2d further indicates that Bi_2S_3 evenly interspersed on the surface of $\text{NH}_2\text{-UiO-66}$ without apparent aggregation.

The detailed morphology and microstructure of $\text{NH}_2\text{-UiO-66}$ and 1.2-BU-S were further investigated by TEM. The typical cubic structure of $\text{NH}_2\text{-UiO-66}$ with a smooth surface and good crystallinity is further confirmed in Fig. 3a. Compared to $\text{NH}_2\text{-UiO-66}$, the UiO-66-S nanocrystals retained the structural feature with C, N, O, Zr and S elements, which are attributed to the reaction of the $-\text{COOH}$ group in thioglycolic

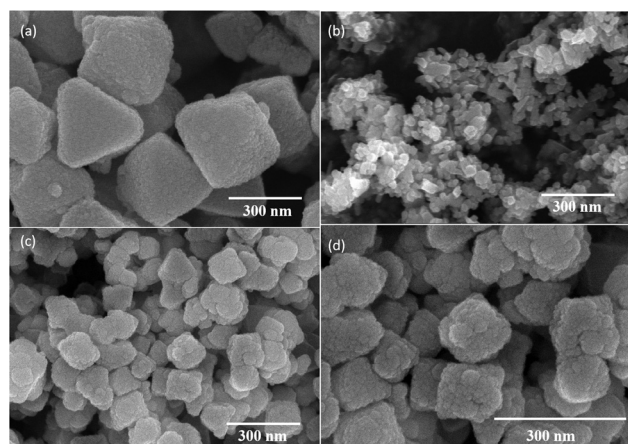


Fig. 2 SEM images of (a) pure $\text{NH}_2\text{-UiO-66}$, (b) pure Bi_2S_3 , and (c) 1.2-BU-S. (d) The high magnification SEM image of 1.2-BU-S.

acid with the $-\text{NH}_2$ group in $\text{NH}_2\text{-UiO-66}$. Observably, the introduction of grafted $-\text{SH}$ from thioglycolic acid by covalent interfacial reaction is beneficial to the further *in situ* self-assembly process with Bi^{3+} ions and the uniform dispersion of Bi_2S_3 NPs on the surface of $\text{NH}_2\text{-UiO-66}$. Fig. 3c shows the TEM images of 1.2-BU-S, which reveal that the $\text{NH}_2\text{-UiO-66}$ nanoparticle is completely encapsulated by Bi_2S_3 . For the 1.2-BU-S composites, C, N, O and Zr elements are evenly distributed in the cubic morphology region corresponding to $\text{NH}_2\text{-UiO-66}$. Furthermore, the strong signals of Bi and S are evenly dispersed on the surface of $\text{NH}_2\text{-UiO-66}$, which are consistent with PXRD and FT-IR analysis results. This conclusion further confirmed that $\text{NH}_2\text{-UiO-66}$, serving as a supporting matrix in the nanocomposites, maintains its structural feature and is uniformly decorated by well-dispersed Bi_2S_3 .

In order to confirm the valence state and content of elements, XPS measurements were conducted on the as-synthesized 1.2-BU-S nanocomposites, and are shown in Fig. 4. For comparison, we also analyzed the XPS spectrum of Bi_2S_3 . As shown in Fig. 4a, the XPS survey spectrum displayed the existence of the Bi, S, Zr,

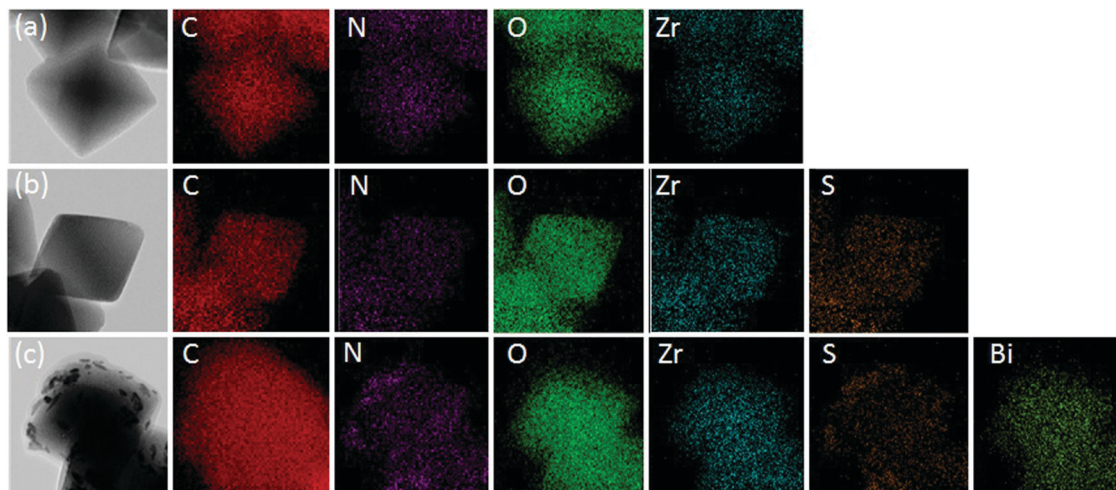


Fig. 3 TEM images and the corresponding elemental mapping analysis of (a) $\text{NH}_2\text{-UiO-66}$, (b) $\text{NH}_2\text{-UiO-66-S}$, (c) 1.2-BU-S.

C, O 1s and N elements, which were consistent with the elemental mapping images (Fig. 4d). For the bare Bi_2S_3 sample, the binding energy peaks at 158.0 eV and 163.3 eV observed for

Bi 4f and the peaks at 161.2 eV and 162.4 eV observed for S 2p were ascribed to the Bi $4f_{7/2}$, Bi $4f_{5/2}$ and S $2p_{3/2}$ and S $2p_{1/2}$ transitions, respectively.^{8,38} Considering the spin orbit

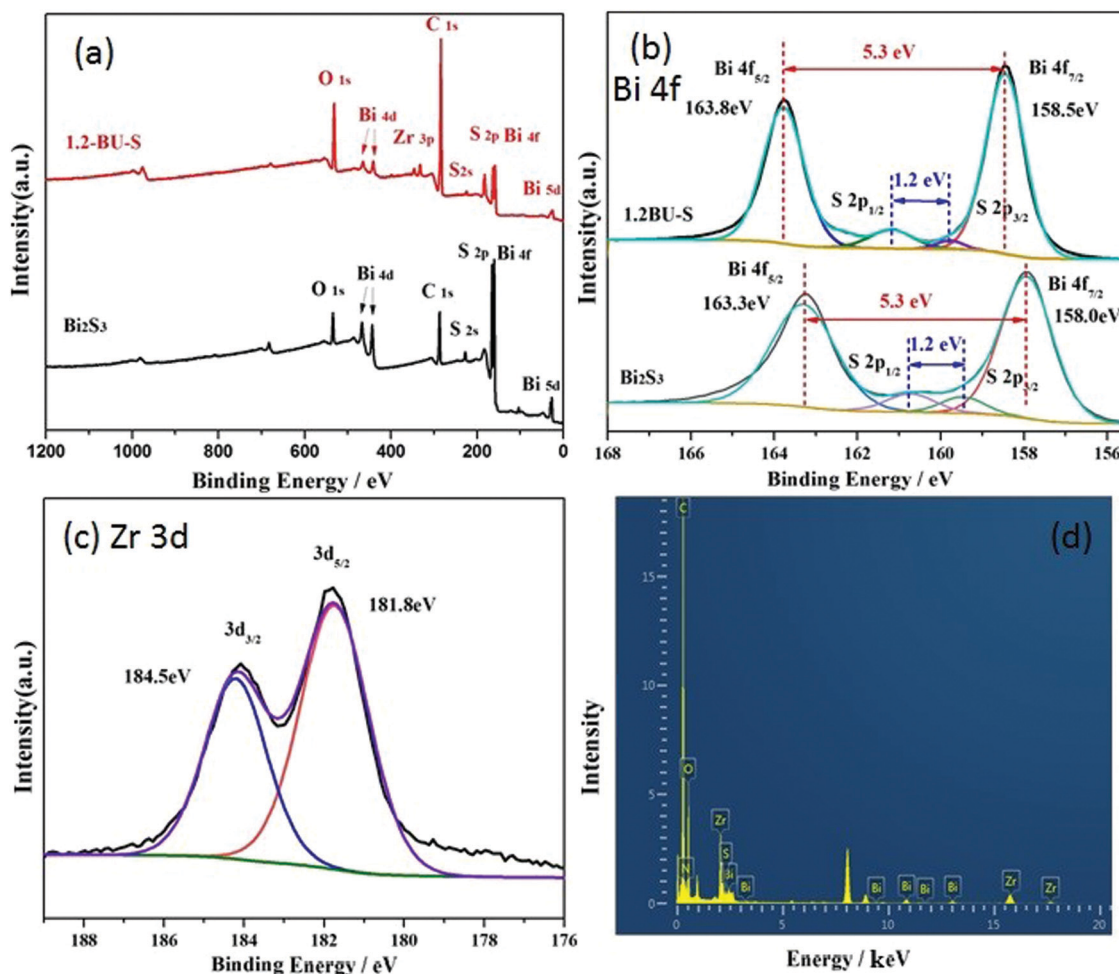


Fig. 4 (a–c) The XPS spectra for 1.2-BU-S: (a) survey scan, (b) high resolution spectra of Bi 4f, (c) high resolution spectra of Zr 3d, (d) the corresponding EDX-mapping of 1.2-BU-S.

separations of 5.3 eV for Bi 4f and 1.2 eV for S 2p, the chemical states of Bi and S were Bi³⁺ and S²⁻ in the Bi₂S₃ sample, which are in accordance with the previous literature.⁷ For 1.2-BU-S, the spin orbit separations of Bi 4f and S 2p are retained, which means the microstructure of Bi₂S₃ in 1.2-BU-S was the same as that found in pure Bi₂S₃. However, the peaks corresponding to Bi 4f_{7/2}, Bi 4f_{5/2}, S 2p_{3/2} and S 2p_{1/2} shift towards higher band energies at 158.5 eV, 163.8 eV, 161.2 eV and 162.4 eV, respectively (Fig. 4b). The shifts mean that Bi₂S₃ not only physically accumulated on the surface of the NH₂-UiO-66 crystals, but a closer interaction is also formed between the Bi^{III} centers and NH₂-UiO-66 frameworks. In Fig. 4c, the peaks observed in the Zr 3d spectra at 181.8 eV and 184.5 eV are attributed to the Zr 3d_{5/2} and Zr 3d_{3/2} core levels, which indicated the existence of Zr⁴⁺.³⁹

3.2. Photocatalytic activities

In order to evaluate the effect of covalent interfacial modification with thioglycolic acid on the synthesis of composites, the as-synthesized novel photocatalysts (*x*-BU-S) were used for the photocatalytic degradation reaction. Methylene blue was selected as a model substrate to study the photocatalytic activities preliminarily, and the photocatalytic experiments in aqueous solution (10 mg L⁻¹) under visible-light irradiation at room temperature were carried out. For comparison, a series of contrast experiments with other photocatalysts were also carried out under similar conditions, such as commercial Degussa P25, 1.2-BU, pristine Bi₂S₃ and the freshly obtained NH₂-UiO-66 sample. As shown in Fig. 5a, the NH₂-UiO-66 sample shows the highest adsorption compared to others due to its large surface area and ordered nanosized channels (Fig. S1 and Table S1, ESI[†]). It is well known that the MB molecule is stable under visible light irradiation, as confirmed by the blank experiment without any photocatalyst. As shown in Fig. 5a, the photodegradation performance was dramatically enhanced and the efficiency increased from 25.3% (observed for the pristine Bi₂S₃) to a maximum of 94.9% for the *x*-BU-S composites after 120 min, and the 1.2-BU-S photocatalyst exhibited the highest degradation effect. Notably, all *x*-BU-S composites showed higher photocatalytic activities compared with the commercial Degussa P25 sample and 1.2-BU composite, implying the potential advantage of post-synthetic modification of NH₂-UiO-66 for the formation of *x*-BU-S composites.

Additionally, we quantified the kinetic behaviors of different photocatalysts in the photodegradation of MB under visible light irradiation. As shown in Fig. 5b, the photodegradation curves suit a pseudo-first order kinetic model expressed by $\ln(C_0/C) = kt$, where C_0 is the initial concentration of MB, C is the concentration of MB after a certain reaction time (t), and k is the relative degradation rate constant. According to the Langmuir-Hinshelwood model, the values of k can be calculated from the slope and the intercept of the linear plot. Compared with the smaller k values for Degussa P25 ($k = 5.7 \times 10^{-4} \text{ min}^{-1}$), 1.2-BU composite without modification ($k = 1.1 \times 10^{-2} \text{ min}^{-1}$) and pristine Bi₂S₃, the obtained *x*-BU-S composited photocatalysts exhibit better photocatalytic activity, showing that the novel synthetic strategy in the photocatalyst could improve the photocatalytic activity. Interestingly, the photocatalytic activity of the 1.2-BU-S composite the highest ($k = 2.3 \times 10^{-2} \text{ min}^{-1}$), and is 12.8 and 40.2 times higher than those of pristine Bi₂S₃ ($1.79 \times 10^{-3} \text{ min}^{-1}$) and Degussa P-25 ($5.7 \times 10^{-4} \text{ min}^{-1}$), respectively. More importantly, the photodegradation efficiency of 1.2-BU-S is about 2 times higher than that of the 1.2-BU composite without post-synthetic modification by thioglycolic acid.

Meanwhile, to determine the reusability of the photocatalyst after photocatalytic reaction, 1.2-BU-S was centrifuged and washed several times with water and ethanol, and reused for the next photocatalytic reaction. As illustrated in Fig. 5c, the high photocatalytic activity of 1.2-BU-S was maintained with only about 3.6% loss in activity observed after 5 cycles, and the photodegradation of MB retained at least 90%. In addition, the PXRD pattern of the recycled catalyst is almost identical to that of the freshly synthesized catalyst, which indicated its outstanding stability (Fig. S2, ESI[†]). It reasonably confirmed that the strong heterojunction formed from the covalent interfacial reaction is responsible for its excellent photostability and photocatalytic property.

3.3. Optical and electrochemical properties

Inspired by the enhanced photocatalytic degradation for the MB dye, we studied the reason for the improved catalytic performance of the novel composites. The UV-Vis DRS of Bi₂S₃, NH₂-UiO-66 and *x*-BU-S are represented in Fig. 6a.

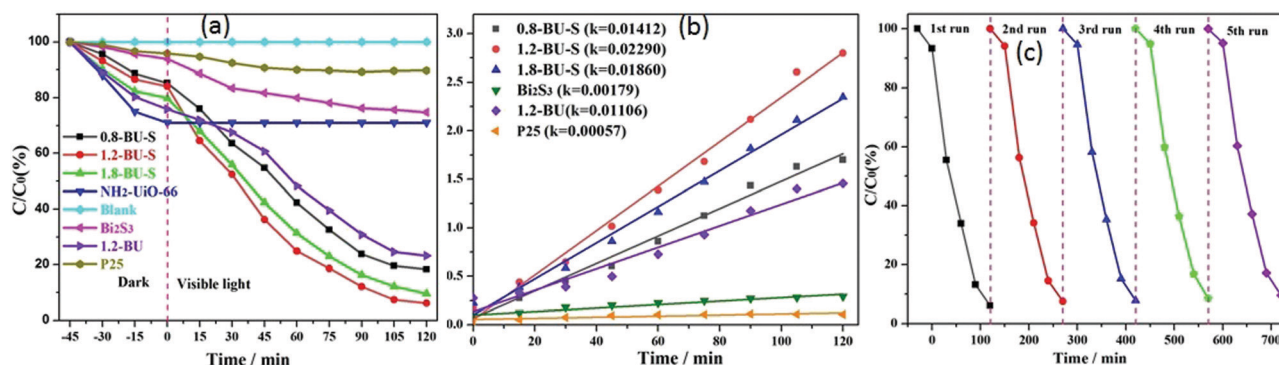


Fig. 5 (a) The photocatalytic activity of the as-synthesized samples; (b) the corresponding kinetics of MB degradation over the different photocatalysts, and (c) the stability of the 1.2-BU-S catalyst over 5 cycles.

As for pure Bi_2S_3 , the absorption range covers the whole UV and visible light region, which indicates the excellent optical response. Moreover, the band gap value is calculated to be 1.56 eV in accordance with the frequency-dependent relationship $ah\nu = (h\nu - E_g)^{1/2}$, as shown in Fig. 6b.⁴⁰ The absorption edge of $\text{NH}_2\text{-UiO-66}$ is located at around 450 nm, and the band gap value is 2.92 eV, demonstrating the capability to utilize visible light. The presence of the $-\text{NH}_2$ group in the BDC^{2-} backbone induces the absorption at wavelengths longer than 300 nm due to the auxochromic and bathochromic shift, which makes $\text{NH}_2\text{-UiO-66}$ a better photocatalyst than UiO-66 .¹⁵ Compared to $\text{NH}_2\text{-UiO-66}$, 1.2-BU-S exhibits an extended absorption in the whole visible light region. Presumably, it originates from the firm combination between $\text{NH}_2\text{-UiO-66}$ and Bi_2S_3 used as a visible-light sensitizer. Therefore, it was concluded that the heterojunction formed from the combination of Bi_2S_3 and $\text{NH}_2\text{-UiO-66}$ was favorable toward the effective utilization of visible light, which suggests that the as-obtained 1.2-BU-S composites are potentially good visible-light-driven photocatalysts.

The transient photocurrent response behaviors in the photocatalytic reaction were carried out to further explore the

separation and transfer efficiency of the photoexcited charge carriers.⁴¹ Fig. 6c shows the photo-induced current with time ($i-t$) curves for all of the samples under visible light irradiation with four intermittent on/off cycles under illumination. The pure Bi_2S_3 nanoparticles showed a very low photocurrent density, which may be due to the fast recombination of photo-generated electrons and holes. This low photocurrent density limited the large scope utilization of the pure Bi_2S_3 nanoparticles for photocatalysis. Notably, all of the obtained x-BU-S composites promptly exhibited remarkably enhanced photocurrent density during the on/off cycles compared to the pristine Bi_2S_3 . More importantly, the stable photocurrent value observed for the 1.2-BU-S sample was the highest among the three composites, suggesting its faster charge separation efficiency, being *ca.* 3.3 times over that of the pristine sample under the same conditions. The extremely high photo-generated current suggests that the separation efficiency of the photogenerated electron-hole pairs of the 1.2-BU-S composites is significantly improved upon the introduction of $\text{NH}_2\text{-UiO-66}$ by post-synthetic modifications, which is responsible for the highest photocatalytic activities.

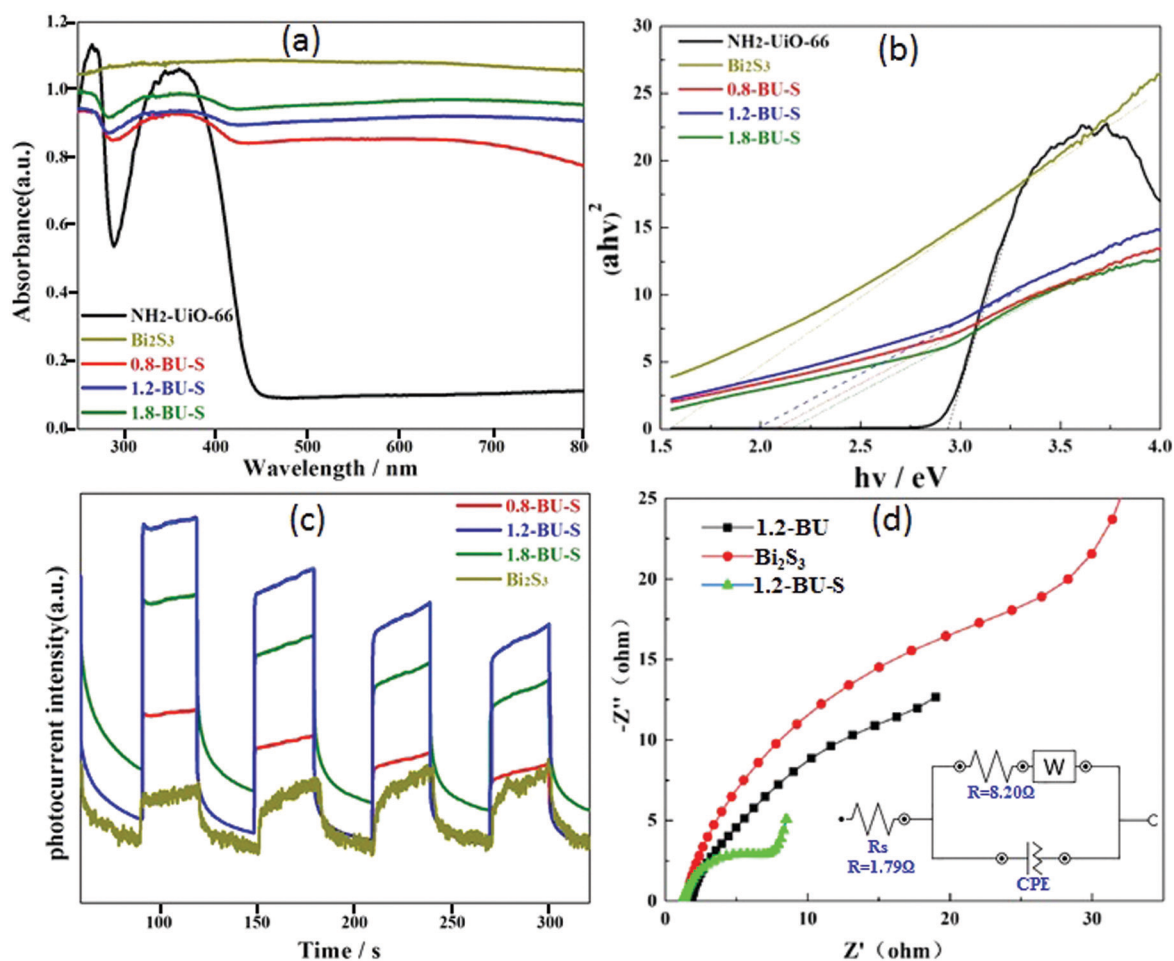


Fig. 6 (a) UV-Vis absorption spectra of the as-synthesized samples and the calculated band gap energies observed for the samples (b). (c) The transient photocurrent responses observed for all samples. (d) EIS spectrum of the Bi_2S_3 , $\text{NH}_2\text{-UiO-66}$, 1.2-BU and 1.2-BU-S, and the Nyquist plots of the catalysts fitted by the RC circuit model (inset figure).

Furthermore, the EIS Nyquist plots of $\text{NH}_2\text{-UiO-66}$, Bi_2S_3 , and 1.2-BU-S were examined to investigate the separation and transfer process of the photoexcited interfacial charges.⁴² As we all know, the smaller radius reflects a lower charge-transfer resistance and higher efficiency of the separation and transfer of the photogenerated charge. As shown in Fig. 6d, 1.2-BU-S exhibited the smallest radius of curvature compared to those of the $\text{NH}_2\text{-UiO-66}$, Bi_2S_3 and $x\text{-BU}$ samples, demonstrating the lower interfacial resistance on the surface of the 1.2-BU-S electrode, which will lead to more efficient charge carrier migration over the hybrid photocatalyst. Meanwhile, the Nyquist plots of the catalysts were also fitted by the RC circuit model, including an internal resistance (as calculated using equivalent series resistance, R_{ESR}) and a charge transfer resistance (R_{ct}) for the electrochemical reaction^{43,44} (inset of Fig. 6d). The simulated R_{ESR} and R_{ct} are shown in Table 1, which reveals that the 1.2-BU-S composites exhibit smaller resistance values than the others, disclosing the optimized charge-transfer capacity of the heterojunction during the photocatalytic degradation process. Obviously, the successful fabrication of $\text{NH}_2\text{-UiO-66}$ and Bi_2S_3 by the covalent interfacial reaction endowed the multicomponent photocatalysts with remarkable reduced arc radii, indicating more effective charge transfer processes.⁴⁵

Photoluminescence (PL) spectroscopy has been used to determine the photophysical characteristics of the photo-generated electrons and holes inside the composites. Fig. 7 shows the PL emission spectra of the as-synthesized samples at

Table 1 The simulated internal resistance (R_{ESR}) and charge transfer resistance (R_{ct}) from the Nyquist plots in Fig. 6d

	Bi_2S_3	1.2-BU	1.2-BU-S
R_{ESR}/Ω	1.41	1.70	1.79
R_{ct}/Ω	16.91	11.09	8.20

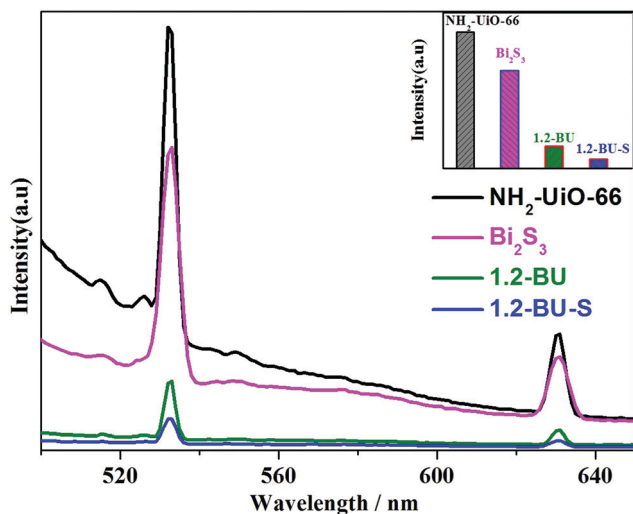


Fig. 7 PL spectra ($\lambda_{\text{ex}} = 435 \text{ nm}$) of the $\text{NH}_2\text{-UiO-66}$, Bi_2S_3 , 1.2-BU and 1.2-BU-S samples and the comparison of the PL intensity (inset).

an excitation wavelength of 435 nm at room temperature. It can be seen that one strong emission peak at about 533 nm can be observed in $\text{NH}_2\text{-UiO-66}$ and pristine Bi_2S_3 , which can be assigned to the direct recombination of photo-generated electrons and holes from the conduction band to valence band. For the 1.2-BU-S and 1.2-BU composites, the emission peaks were similar to those of pure Bi_2S_3 , but the intensity decreased remarkably, indicating the low recombination rate of the photo-generated electrons and holes in these composites.⁴⁶ The results showed that the recombination of Bi_2S_3 NPs and the $\text{NH}_2\text{-UiO-66}$ system provided extra pathways for the migration of photo-generated electrons, suppressing the recombination rate. Moreover, the PL intensity of the 1.2-BU-S sample is weakest (the inset of Fig. 7), suggesting the highest separation efficiency of the charge carriers responsible for the enhanced photocatalytic performance, which is in agreement with the observed photocatalytic performances.

3.4. Photocatalytic mechanism

To gain insight into the mechanism of the photocatalytic reaction, the reactive species trapping experiments were first carried out to detect the active species generated during the photocatalytic degradation process. It is well known that superoxide anion radicals ($\cdot\text{O}_2^-$), holes (h^+), and hydroxyl radicals ($\cdot\text{OH}$) are the three main active species involved in the heterogeneous photocatalytic reaction process.⁵¹ In order to further confirm the active species in the photocatalytic systems, isopropyl alcohol (IPA), *para*-benzoquinone (p-BQ), and ethylenediaminetetraacetic acid disodium (EDTA-Na) were selected as scavengers for the photogenerated $\cdot\text{OH}$, $\cdot\text{O}_2^-$, and h^+ , respectively.⁴⁷ The influence of different scavengers on the photo-degradation reaction is shown in Fig. 8a. Photocatalytic degradation of MB drastically decreased after adding EDTA-Na and p-BQ, while only a slight influence on suppressing the photocatalytic activity was observed after adding IPA, indicating that $\cdot\text{OH}$ is not the active species in the reaction. These results confirm the crucial role of the holes and $\cdot\text{O}_2^-$ toward the photocatalytic degradation of MB from the direct interaction between the photogenerated electron and absorbed oxygen molecules on the photocatalyst surface ($\text{O}_2 + \text{e}^- \rightarrow \cdot\text{O}_2^-$), which are in accordance with the reported literature.⁴⁸ The free electrons can react with the absorbed oxygen molecules and create $\cdot\text{O}_2^-$, which can react with the dye molecules. In addition, the MB photodegradation efficiency in the presence of p-BQ and EDTA-Na was inferior to that found with no scavenger, indicating that the generation of $\cdot\text{O}_2^-$ and h^+ play dominant roles in the photocatalytic reaction. Furthermore, the electron-spin-resonance (ESR) experiments were performed to give direct proof of $\cdot\text{O}_2^-$. 5,5-Dimethyl-1-pyrroline-*N*-oxide (DMPO) was employed as sensitive trapping agents for $\cdot\text{O}_2^-$ in both reactions. As shown in Fig. 8b, the typical peaks of $\cdot\text{O}_2^-$ were observed under visible-light irradiation, whereas no signal can be detected without light irradiation in the presence of DMPO, suggesting the existence of $\cdot\text{O}_2^-$. Meanwhile, the $\cdot\text{O}_2^-$ peaks on ESR decreased significantly when the reaction substrate of MB was added into the suspension, demonstrating the major role of $\cdot\text{O}_2^-$ in the photocatalytic

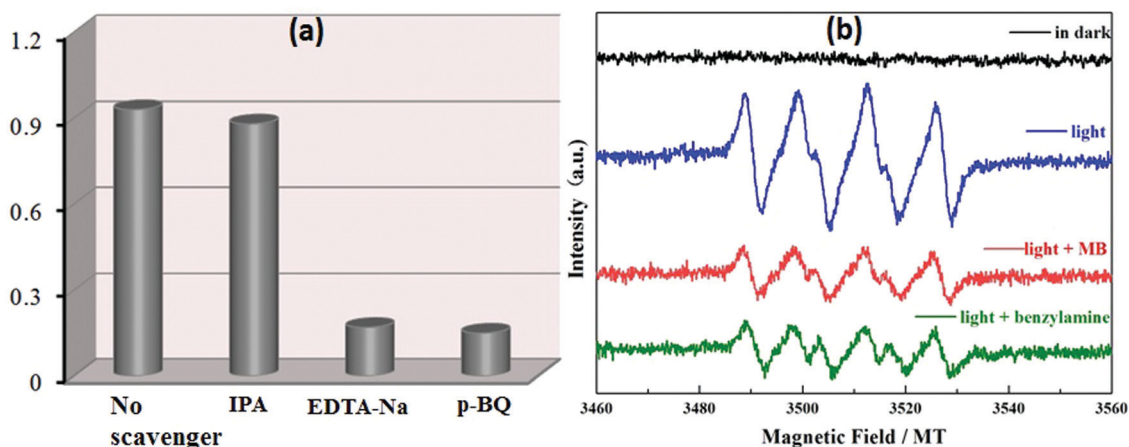


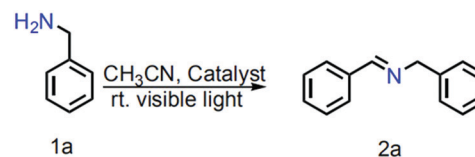
Fig. 8 (a) The trapping experiments of the active species on the degradation of MB in the presence of 1.2-BU-S under visible-light irradiation. (b) ESR spectra of the 1.2-BU-S sample before and after visible-light irradiation in the degradation of MB and oxidative coupling of benzylamine.

process, which is consistent with the results from the trapping experiments.

Based on the above analysis, a possible photocatalytic mechanism of 1.2-BU-S was elucidated using the following empirical formulae ($E_{CB} = E_{VB} + E_g$) (Fig. 9). Generally, the photocatalytic properties of a catalyst are associated with its band structure.⁴⁹ The visible light irradiation of the photocatalyst caused Bi_2S_3 and $\text{NH}_2\text{-UiO-66}$ to be excited simultaneously. The photo-generated electrons (e^-) can be excited from the highest VB to enter its lowest CB, leaving the holes (h^+) in the VB. Notably, the conduction band (CB) edge potentials in Bi_2S_3 (-0.99 eV) had more negative potential compared to $\text{NH}_2\text{-UiO-66}$ (-0.60 eV) versus the normal hydrogen electrode (NHE).^{28,50} On the other hand, the highest occupied molecular orbital (HOMO) of $\text{NH}_2\text{-UiO-66}$ (2.32 eV) had a more positive potential than that of Bi_2S_3 (0.57 eV). Thus, the photoelectrons in the lowest unoccupied molecular orbital (LUMO) of $\text{NH}_2\text{-UiO-66}$ are inclined to transfer to the Bi_2S_3 NPs. Meanwhile, the produced holes (h^+) from the Bi_2S_3 NPs can migrate to the VB of $\text{NH}_2\text{-UiO-66}$, owing to their intimate interfacial contact. This process could efficiently separate the electrons and suppress electron-hole recombination. Therefore, the photogenerated electrons concentrate on the CB of the interfacial Bi_2S_3 NPs

anchored on $\text{NH}_2\text{-UiO-66}$ by post-synthetic modifications, which are trapped by the adsorbed molecular oxygen in solution, generating the highly active $\cdot\text{O}_2^-$. The effective separation and transfer of the charge carriers through the more intimate interface make the 1.2-BU-S heterojunction demonstrate more efficient photocatalytic performance.

Inspired by the excellent visible-light absorption and stability of the $x\text{-BU-S}$ composites, we tested the photocatalytic oxidative coupling of the amines to yield imines (Scheme 2). It is well known that imines and their derivatives are important N-containing active intermediates in the synthesis of drugs and other fine chemicals. Traditionally, they are synthesized by aldehyde-amine condensation using unstable aldehydes, Lewis acid catalysts, toxic oxidants and dehydrating agents.^{51,52} Considering the demand for green chemistry and sustainable



Scheme 2 The oxidative coupling of benzylamine photocatalyzed by 1.2-BU-S.

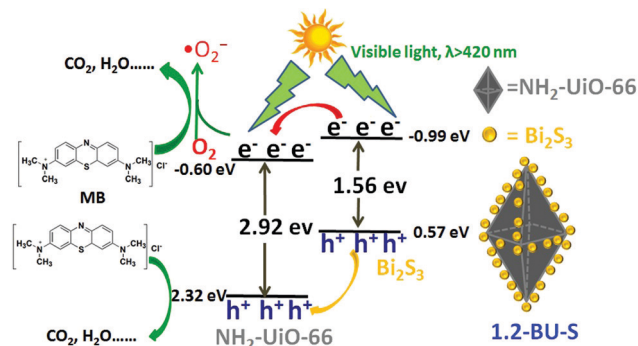
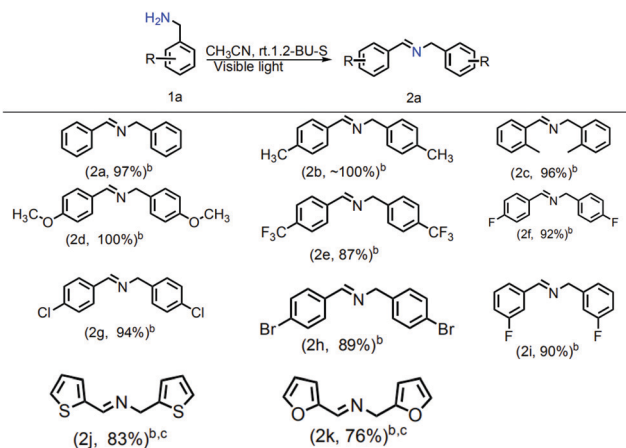


Fig. 9 The proposed photocatalytic mechanism for the MB degradation of 1.2-BU-S under visible-light irradiation.

Table 2 The oxidative coupling of benzylamine photocatalyzed by 1.2-BU-S^a

Entry	Catalyst	Temp. (°C)	Time (h)	Oxidant	Conversion ^b (%)
1	No catalyst	R.T.	12	Air	0
2	1.2-BU-S, in dark	r.t.	2	Air	0
3	1.2-BU-S	r.t.	3	Air	97
4	1.2-BU-S	r.t.	3	O ₂	~100
5 ^c	1.2-BU-S	Refluxing	6	Ar	<2
6 ^d	1.2-BU-S	r.t.	3	Air	95

^a Reaction condition: benzylamine (0.5 mmol), CH_3CN (5 mL) as the solvent, room temperature for 3 h under irradiation with visible light ($\lambda > 420$ nm), 1.2-BU-S (10 mg), n -dodecane (100 μL , as the internal standard), air balloon. ^b Yields were determined by GC area. ^c Refluxing for 6 h. ^d After the 5th recycle.

Table 3 The oxidative coupling of benzylamine and its derivatives to the corresponding imines catalyzed by 1.2-BU-S^a

^a All reactions were carried out under the optimized conditions: benzylamine (0.5 mmol), CH₃CN (5 mL) as the solvent, room temperature for 3 h under irradiation with visible light ($\lambda > 420$ nm), catalyst (10 mg), *n*-dodecane (100 μ L, as the internal standard), air balloon. ^b Conversions were determined by the GC area. ^c At room temperature for 12 h.

development, the direct photocatalytic oxidation of amines is a hot topic nowadays.^{53,54} In 2015, Li and co-workers found that NH₂-MIL-125(Ti) exhibited photocatalytic activity for the aerobic

selective oxidation of amines to imines for the first time. Until now, some MOF-based photocatalysts have been employed for the oxidative coupling of amines (such as PCN-222, Zn-PDI and FJI-Y10).^{55–58} Here, benzylamine was selected as a model substrate to optimize the oxidative coupling reaction conditions. As reported in the literature, the reaction was first conducted under air atmosphere with CH₃CN as the solvent. Of course, a series of control experiments were also conducted. As shown in Table 2, the blank experiment without any catalysts showed negligible conversion (<1% conversion), even after 12 h of reaction time. Meanwhile, a higher conversion (>97%) was obtained in the presence of the 1.2-BU-S catalyst in a shorter reaction time (3 h) under similar conditions. It can be realized that 1.2-BU-S was highly effective in catalyzing the oxidative coupling reaction of benzylamine. Meanwhile, the oxidative coupling reaction cannot proceed without light irradiation (Table 2, entry 2), indicating that the oxidation coupling is due entirely to a photocatalytic reaction. The use of air and pure O₂ as an oxidant had no significant influence on the reaction (Table 2, entries 3 and 4), which indicated that the participation of O₂ is not involved in the rate-determining steps. However, only a trace amount of benzylidenebenzylamine product was observed (<2%, Table 1, entry 5) when the reaction was carried out under Ar balloon with refluxing for 6 h. In addition, the cycling experiments showed almost identical photocatalytic

Table 4 Photocatalytic oxidation of benzylamine to imine over different MOFs-based catalysts

Entry	Catalyst	Light source	Conditions	Conversion	TOF ^a μ mol g ⁻¹ h ⁻¹	Ref.
1	PCN-222	Xe lamp ($\lambda > 420$ nm)	r.t. air, 1 h, 0.1 mmol benzylamine, 5 mg PCN-222, 3 mL CH ₃ CN	100%	10 000	55
2	NH ₂ -MIL-125 (Ti)	visible light	r.t. O ₂ , 12 h, 0.1 mmol benzylamine, 5 mg catalyst, 2 mL CH ₃ CN	73%	608	56
3	Zn-PDI	Xe lamp (500 W) ($\lambda > 420$ nm)	r.t. air, 4 h, 1 mmol benzylamine, 0.01 mmol Zn-PDI, 5 mL CH ₃ CN	74%	9935	57
4	FJI-Y10	Xe lamp (300 W) ($\lambda > 420$ nm)	40 °C, O ₂ , 6 h, 1.0 mmol benzylamine, 10 mg FJI-Y10, 5 mL DMF	100%	8333	58
5	Zn-MOF	Xe arc lamp (300 W) ($\lambda > 420$ nm)	r.t. O ₂ , 1 h, 0.2 mmol benzylamine, 5 mg Zn-MOF, 1 mL CH ₃ CN	99%	19 800	59
6	Zn-bpydc	Xe lamp (300 W) with full spectrum	25 °C, air, 4 h, 0.5 mmol benzylamine, 10 mg Zn-bpydc, 5 mL DMF	99.7%	6231	60
7	Mn-MOF	Xe lamp (300 W) (420 < λ < 800 nm)	r.t. O ₂ , 1 h, 0.2 mmol benzylamine, 6 mg Mn-MOF, 1 mL DMA/DMF (v/v = 1/1)	99%	16 500	61
8	Cd(dcbpy)	Xe lamp (300 W) with full spectrum	25 °C, air, 7 h, 0.48 mmol benzylamine, 10 mg catalyst, 5 mL DMF	99%	3398	62
9	RPF-30-Er	100 W warming lamp	25 °C, O ₂ , 18 h, 0.05 mmol benzylamine, 10 mol% catalyst, 1 mL CH ₃ CN	76%	71	63
10	NNU-45	Xe lamp (300 W) ($\lambda > 420$ nm)	r.t. O ₂ , 160 min, 0.2 mmol benzylamine, 4 mg catalyst, 1 mL DMSO	99%	9281	64
11	NH ₂ -UiO-66	Xe lamp (350 W) with full spectrum	r.t. air, 10 h, 0.1 mmol benzylamine, 15 mg NH ₂ -UiO-66, 5 mL CH ₃ CN	83%	277	65
12	Pd(1.0)/MIL-125-NH ₂	Xe lamp (300 W) 360–780 nm	r.t. O ₂ , 3 h, 0.05 mmol benzylamine, 5 mg photocatalyst, 2 mL CH ₃ CN	94.08%	3136	66
13	Ru(bpy) ₃ @MIL-125	Xe lamp (300 W) ($\lambda > 440$ nm)	r.t. air, 3 h, 0.1 mmol benzylamine, 5 mg catalyst, 3 mL CH ₃ CN	100%	3333	67
14	CNUIO-5	Xe lamp (300 W) ($\lambda > 420$ nm)	r.t. O ₂ , 5 h, 0.05 mmol benzylamines, 5 mg CNUIO-5, 5 mL CH ₃ CN	58.9%	589	68
15	CdS@MIL-101	Xe lamp (300 W) ($\lambda > 420$ nm)	Ice bath, air, 9 h, 0.1 mmol benzylamine, 50 mg catalyst, 2 mL toluene	100%	111	69
16	1.2-BU-S	Xe lamp (300 W) ($\lambda > 420$ nm)	Ice bath, air, 3 h, 0.5 mmol benzylamine, 10 mg 1.2-BU-S, 5 mL CH ₃ CN	97%	8083	This work

^a TOF = mmol of amine conversion converted per gram of catalyst per hour.

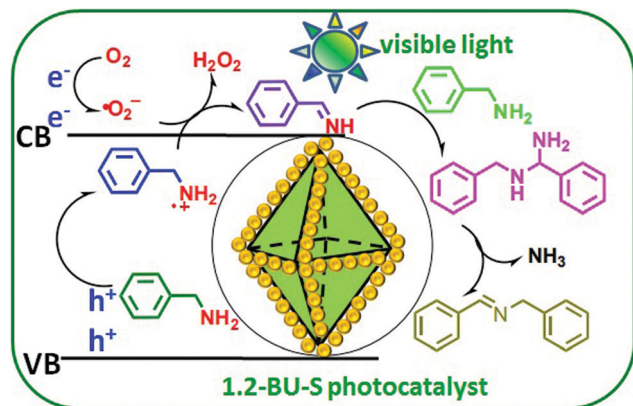


Fig. 10 The proposed photocatalytic mechanism for the oxidative coupling reaction with 1.2-BU-S under visible-light irradiation.

efficiency after five times of reuse (Table 2, entry 6). Although some MOFs have been explored as catalysts for the oxidation of amine, a longer time and higher temperature were usually necessary in order to afford good conversions and selectivity, and only a few MOF-based photocatalysts have been applied for the oxidative coupling of amine. The 1.2-BU-S sample showed good activity (>97% conversion) in a shorter reaction time (3 h) and low temperature in the oxidation of the benzylamine reaction. The turnover frequency (TOF) of the reaction was estimated to be about $8083 \mu\text{mol g}_{\text{cat}}^{-1} \text{h}^{-1}$, which is among the best MOF-based photocatalysts for the oxidative coupling reaction. A comparison of the catalytic performance of the 1.2-BU-S heterojunction with the reported photocatalysts is listed in Table 4. Its photocatalytic efficiency is superior to those of the pure MOF photocatalysts, such as FJI-Y10, $\text{NH}_2\text{-MIL-125}(\text{Ti})$, $\text{Cd}(\text{dcbpy})$, RPF-30-Er, $\text{NH}_2\text{-UiO-66}$ and some of the reported noble metal supported MOF catalysts, including $\text{Ru}(\text{bpy})_3@ \text{MIL-125}$ and $\text{Pd}(1.0)/\text{MIL-125-NH}_2$.^{55–69}

Based on the optimized conditions by using benzylamine as a model substrate, we examined the general applicability of the photocatalytic oxidative coupling for different substrates bearing various functional groups (H, Me, OMe, CF_3 , F and Cl). As shown in Table 3, the 1.2-BU-S catalyst can catalyze the photocatalytic oxidative coupling of benzylamine and its derivatives with both electron-withdrawing and electron-donating groups, and yield corresponding imines with high conversion (>87%). On the whole, the substituent on the phenyl ring has an insignificant effect on the reaction conversion, and the substrate with electron-donating groups (such as $-\text{Me}$, $-\text{OMe}$) led to higher conversion than the electron-withdrawing groups, such as $-\text{X}$ ($\text{X} = \text{F}, \text{Cl}, \text{Br}$ and CF_3) groups.⁷⁰ In addition, the oxidative coupling of heterocyclic amines, *e.g.*, 2-furfurylamine and 2-thiophenemethanamine, provided the corresponding imines with good yields, but with much decreased reaction rate and conversion, consistent with the previous results.

For the oxidative coupling of benzylamine photocatalyzed by the 1.2-BU-S catalyst, the proposed mechanism is displayed in Fig. 10, which is similar to the photodegradation of MB.

As shown by ESR measurements, the $\bullet\text{O}_2^-$ signals on ESR decreased remarkably when benzylamine was added to the suspension, meaning that the generated $\bullet\text{O}_2^-$ plays an important role in the oxidative coupling of benzylamine. The reaction is also launched from the generation of the photo-induced electron (e^-) and holes (h^+). Under light irradiation, benzylamine interacts with the photogenerated holes to form radical $\text{PhCH}_2\text{NH}_2^{\bullet+}$ cations, which are further oxidized by the formed superoxide radicals to give the highly active $\text{PhCH}=\text{NH}$ intermediate. Afterwards, the active $\text{PhCH}=\text{NH}$ intermediate and benzylamine further undergo a condensation reaction to generate the coupled imine product.^{58–61} As a result, the effective separation and transfer of the photogenerated electron and holes contribute to the excellent photocatalytic activity of the 1.2-BU-S heterojunction. Furthermore, the intimate interfacial covalent interaction by thioglycolic acid modification makes it more effective, and thus boosts the photocatalytic oxidative coupling process.

5. Conclusions

In this paper, Bi_2S_3 -modified $\text{NH}_2\text{-UiO-66}$ composites were reported by the covalent interfacial reaction. The novel composites can be used as a heterogeneous photocatalyst to photodegrade methylene blue (MB), and for the oxidative coupling of primary benzylamine and its derivatives into corresponding imines. The *x*-BU-S composites display enhanced photocatalytic performance under visible light irradiation compared to pristine $\text{NH}_2\text{-UiO-66}$, Bi_2S_3 and reported photocatalysts, which are attributed to the more intimate interface by the covalent interfacial reaction. The quenching test and ESR experiments revealed that main important agent during photocatalytic reaction is $\bullet\text{O}_2^-$. Based on the above result, the work in this paper provides a new avenue for the design of MOF-based composites.

Author contributions

The manuscript was written through the contributions of all authors. All authors have given approval to the final version of the manuscript.

Conflicts of interest

The authors declare no competing financial interest.

Acknowledgements

This work is supported by the National Natural Science Foundation of China (51472162 and 21707093), the Foundation of Science and Technology Commission of Shanghai Municipality (18090503600 and 20190503300), and Chemical Engineering and Technology (Perfume and Aroma Technology) of Shanghai Plateau Discipline.

References

- 1 A. Kaur, A. Umar and S. K. Kansal, Heterogeneous photocatalytic studies of analgesic and non-steroidal anti-inflammatory drugs, *Appl. Catal., A*, 2016, **510**, 134–155.
- 2 H. Tong, S. Ouyang, Y. Bi, N. Umezawa, M. Oshikiri and J. Ye, Nano-photocatalytic Materials: Possibilities and Challenges, *Adv. Mater.*, 2012, **24**, 229–251.
- 3 D. Chen, Z. Wang, T. Ren, H. Ding, W. Yao, R. Zong and Y. Zhu, Influence of Defects on the Photocatalytic Activity of ZnO, *J. Phys. Chem. C*, 2014, **118**, 15300–15307.
- 4 D. Shao, H. Sun, J. Gao, G. Xin, M. Anthony Aguilar, T. Yao, N. Koratkar, J. Lian and S. Sawyer, Flexible, Thorn-like ZnO-multiwalled Carbon Nanotube Hybrid Paper for Efficient Ultraviolet Sensing and Photocatalyst Applications, *Nanoscale*, 2014, **6**, 13630–13636.
- 5 S. Akilandeswari, G. Rajesh, D. Govindarajan, K. Thirumalai and M. Swaminathan, Efficacy of photoluminescence and photocatalytic properties of Mn doped ZrO₂ nanoparticles by facile precipitation method, *J. Mater. Sci.: Mater. Electron.*, 2018, **29**, 18258–18270.
- 6 Y. He, D. Li, G. Xiao, W. Chen, Y. Chen, M. Sun, H. Huang and X. Fu, A new application of nanocrystal In₂S₃ in efficient degradation of organic pollutants under visible light irradiation, *J. Phys. Chem. C*, 2009, **113**(13), 5254–5262.
- 7 Y. Luo, H. Chen, X. Li, Z. Gong, X. Wang, X. Peng, M. He and Z. Sheng, Wet chemical synthesis of Bi₂S₃ nanorods for efficient photocatalysis, *Mater. Lett.*, 2013, **105**, 12–15.
- 8 D.-N. Xiong, G.-F. Huang, B.-X. Zhou, Q. Yan, A.-L. Pan and W.-Q. Huang, Facile ion-exchange synthesis of mesoporous Bi₂S₃/ZnS nanoplate with high adsorption capability and photocatalytic activity, *J. Colloid Interface Sci.*, 2016, **464**, 103–109.
- 9 H. Wang, X. Yuan, Y. Wu, G. Zeng, X. Chen, L. Leng and H. Li, Synthesis and applications of novel graphitic carbon nitride/metal-organic frameworks mesoporous photocatalyst for dyes removal, *Appl. Catal., B*, 2015, **174–175**, 445–454.
- 10 H. Sudrajat, A one-pot, solid-state route for realizing highly visible light active Na-doped g-C₃N₄ photocatalysts, *J. Solid State Chem.*, 2018, **257**, 26–33.
- 11 W.-J. Ong, L.-L. Tan, Y. H. Ng, S.-T. Yong and S.-P. Chai, Graphitic Carbon Nitride (g-C₃N₄)-Based Photocatalysts for Artificial Photosynthesis and Environmental Remediation: Are We a Step Closer To Achieving Sustainability?, *Chem. Rev.*, 2016, **116**, 7159–7329.
- 12 Y. Pi, X. Li, Q. Xia, J. Wu, Y. Li, J. Xiao and Z. Li, Adsorptive and photocatalytic removal of Persistent Organic Pollutants (POPs) in water by metal-organic frameworks (MOFs), *Chem. Eng. J.*, 2018, **337**, 351–371.
- 13 H. Wang, N. Zhang, S.-M. Li, Q.-F. Ke, Z.-Q. Li and M. Zhou, Metal-organic framework composites for energy conversion and storage, *J. Semicond.*, 2020, **41**(9), 091707.
- 14 A. Dhakshinamoorthy, A. M. Asiri and H. Garcia, Metal Organic Framework (MOF) Compounds: Photocatalysts for Redox Reactions and Solar Fuel Production, *Angew. Chem., Int. Ed.*, 2016, **55**, 5414–5445.
- 15 J.-D. Xiao and H.-L. Jiang, Metal-Organic Frameworks for Photocatalysis and Photothermal Catalysis, *Acc. Chem. Res.*, 2019, **52**(2), 356–366.
- 16 Y. Horiuchi, T. Toyao, M. Saito, K. Mochizuki, M. Iwata, H. Higashimura, M. Anpo and M. Matsuoka, Visible-Light-Promoted Photocatalytic Hydrogen Production by Using an Amino-Functionalized Ti(IV) Metal-Organic Framework, *J. Phys. Chem. C*, 2012, **116**, 20848–20853.
- 17 L. Wu, Y. Tong, L. Gu, Z.-M. Xue and Y. Yuan, MOFs as an electron-transfer-bridge between a dye photosensitizer and a low cost Ni₂P co-catalyst for increased photocatalytic H₂ generation, *Sustain. Energy Fuels*, 2018, **2**(11), 2502–2506.
- 18 D. Sun, Y. Fu, W. Liu, L. Ye, D. Wang, L. Yang, P. Fu and P. Li, Studies on Photocatalytic CO₂ Reduction over NH₂-UiO-66(Zr) and Its Derivatives: Towards a Better Understanding of Photocatalysis on Metal-Organic Frameworks, *Chem. – Eur. J.*, 2013, **19**, 14279–14285.
- 19 K. G. Laurier, F. Vermoortele, R. Ameloot, D. E. De Vos, J. Hofkens and M. B. Roeloffs, Iron(III)-Based Metal-Organic Frameworks As Visible Light Photocatalysts, *J. Am. Chem. Soc.*, 2013, **135**, 14488–14491.
- 20 G. Wang, Q. Sun, Y. Liu, B. Huang, Y. Dai, X. Zhang and X. Qin, A Bismuth-Based Metal-Organic Framework as an Efficient Visible-Light-Driven Photocatalyst, *Chem. – Eur. J.*, 2014, **21**, 2364–2367.
- 21 Y. Fu, D. Sun, Y. Chen, R. Huang, Z. Ding, X. Fu and Z. Li, An Amine-Functionalized Titanium Metal-Organic Framework Photocatalyst with Visible-Light-Induced Activity for CO₂ Reduction, *Angew. Chem., Int. Ed.*, 2012, **51**, 3364–3367.
- 22 Z. Sha, H. S. O. Chan and J. Wu, Ag₂CO₃/UiO-66(Zr) composite with enhanced visible-light promoted photocatalytic activity for dye degradation, *J. Hazard. Mater.*, 2015, **299**, 132–140.
- 23 J. Ding, Z. Yang, C. He, X. Tong and Y. Li, UiO-66(Zr) coupled with Bi₂MoO₆ as photocatalyst for visible-light promoted dye degradation, *J. Colloid Interface Sci.*, 2017, **497**, 126–133.
- 24 X.-Y. Lin, Y.-H. Li, M.-Y. Qi, Z.-R. Tang, H.-L. Jiang and Y.-J. Xu, A unique coordination-driven route for the precise nanoassembly of metal sulfides on metal-organic frameworks, *Nanoscale Horiz.*, 2020, **5**(4), 714–719.
- 25 N. Zhang, X. Zhang, C. Gan, J. Zhang, Y. Liu, M. Zhou, C. Zhang and Y. Fang, Heterostructural Ag₃PO₄/UiO-66 composite for highly efficient visible-light photocatalysts with long-term stability, *J. Photochem. Photobiol., A*, 2019, **376**, 305–315.
- 26 H. Wang, P.-H. Cui, J.-X. Shi, J.-Y. Tan, J.-Y. Zhang, N. Zhang and C. Zhang, Controllable self-assembly of CdS@NH₂-MIL-125(Ti) heterostructure with enhanced photodegradation efficiency for organic pollutants through synergistic effect, *Mater. Sci. Semicond. Process.*, 2019, **97**, 91–100.
- 27 C. Gan, C. Xu, H. Wang, N. Zhang, J. Zhang and Y. Fang, Facile synthesis of rGO@In₂S₃@UiO-66 ternary composite with enhanced visible-light photodegradation activity for methyl orange, *J. Photochem. Photobiol., A*, 2019, **384**, 112025.

- 28 Y.-H. Ding, X.-L. Zhang, N. Zhang, J.-Y. Zhang, R. Zhang, Y.-F. Liu and Y.-Z. Fang, Visible-light driven Bi_2S_3 @ZIF-8 core-shell heterostructure and synergistic photocatalysis mechanism, *Dalton Trans.*, 2018, **47**, 684–692.
- 29 X. Zhang, N. Zhang, C. Gan, Y. Liu, L. Chen, C. Zhang and Y. Fang, Synthesis of In_2S_3 /UiO-66 hybrid with enhanced photocatalytic activity towards methyl orange and tetracycline hydrochloride degradation under visible-light irradiation, *Mater. Sci. Semicond. Process.*, 2019, **91**, 212–221.
- 30 C. G. Silva, I. Luz, F. X. Llabres i Xamena, A. Corma and H. Garcia, Water Stable Zr-Benzenedicarboxylate Metal–Organic Frameworks as Photocatalysts for Hydrogen Generation, *Chem. – Eur. J.*, 2010, **16**, 11133–11138.
- 31 K. Užarević, T. C. Wang, S.-Y. Moon, A. M. Fidelli, J. T. Hupp, O. K. Farha and T. Friščić, Mechanochemical and solvent-free assembly of zirconium-based metal–organic frameworks, *Chem. Commun.*, 2016, **52**, 2133–2136.
- 32 Y. Su, Z. Zhang, H. Liu and Y. Wang, $\text{Cd}_{0.2}\text{Zn}_{0.8}\text{S}$ @UiO-66- NH_2 nanocomposites as efficient and stable visible-light-driven photocatalyst for H_2 evolution and CO_2 reduction, *Appl. Catal., B*, 2017, **200**, 448–457.
- 33 Q. Liang, S. Cui, C. Liu, S. Xu, C. Yao and Z. Li, Construction of CdS @UiO-66- NH_2 core-shell nanorods for enhanced photocatalytic activity with excellent photostability, *J. Colloid Interface Sci.*, 2018, **524**, 379–387.
- 34 L. Wang, P. Zheng, X. Zhou, M. Xu and X. Liu, Facile fabrication of CdS /UiO-66- NH_2 heterojunction photocatalysts for efficient and stable photodegradation of pollution, *J. Photochem. Photobiol., A*, 2019, **376**, 80–87.
- 35 Y. Luo, H. Chen, X. Li, Z. Gong, X. Wang, X. Peng, M. He and Z. Sheng, Wet chemical synthesis of Bi_2S_3 nanorods for efficient photocatalysis, *Mater. Lett.*, 2013, **105**, 12–15.
- 36 M. Kandiah, S. Usseglio, S. Svelle, U. Olsbye, K. P. Lillerud and M. Tilset, Post-synthetic modification of the metal–organic framework compound UiO-66, *J. Mater. Chem.*, 2010, **20**, 9848–9851.
- 37 L. Shen, W. Wu, R. Liang, R. Lin and L. Wu, Highly dispersed palladium nanoparticles anchored on UiO-66(NH_2) metal–organic framework as a reusable and dual functional visible-light-driven photocatalyst, *Nanoscale*, 2013, **5**, 9374–9382.
- 38 S. Adhikari and D.-H. Kim, Synthesis of Bi_2S_3 / Bi_2WO_6 hierarchical microstructures for enhanced visible light driven photocatalytic degradation and photoelectrochemical sensing of ofloxacin, *Chem. Eng. J.*, 2018, **354**, 692–705.
- 39 J.-D. Xiao, Q. Shang, Y. Xiong, Q. Zhang, Y. Luo, S.-H. Yu and H.-L. Jiang, Boosting Photocatalytic Hydrogen Production of a Metal–Organic Framework Decorated with Platinum Nanoparticles: The Platinum Location Matters, *Angew. Chem., Int. Ed.*, 2016, **55**, 9389–9393.
- 40 S. Abdpour, E. Kowsari, M. R. A. Moghaddam, L. Schmolke and C. Janiak, MIL-100(Fe) nanoparticles supported on urchin like Bi_2S_3 structure for improving photocatalytic degradation of rhodamine-B dye under visible light irradiation, *J. Solid State Chem.*, 2018, **266**, 54–62.
- 41 L. Jing, Y. Xu, M. Xie, J. Liu, J. Deng, L. Huang, H. Xu and H. Li, Three dimensional polyaniline/ MgIn_2S_4 nanoflower photocatalysts accelerated interfacial charge transfer for the photoreduction of $\text{Cr}(\text{VI})$, photodegradation of organic pollution and photocatalytic H_2 production, *Chem. Eng. J.*, 2019, **360**, 1601–1612.
- 42 J.-D. Xiao and H.-L. Jiang, Thermally Stable Metal–Organic Framework-Templated Synthesis of Hierarchically Porous Metal Sulfides: Enhanced Photocatalytic Hydrogen Production, *Small*, 2017, **13**, 1700632.
- 43 Y. Wen, T. E. Rufford, D. Hulicova-Jurcakova and L. Wang, Nitrogen and Phosphorous Co-Doped Graphene Monolith for Supercapacitors, *ChemSusChem*, 2016, **9**, 513–520.
- 44 M. Chauhan, K. P. Reddy, C. S. Gopinath and S. Deka, Copper Cobalt Sulfide Nanosheets Realizing a Promising Electrocatalytic Oxygen Evolution Reaction, *ACS Catal.*, 2017, **7**, 5871–5879.
- 45 X. Peng, L. Ye, Y. Ding, L. Yi, C. Zhang and Z. Wen, Nanohybrid photocatalysts with ZnIn_2S_4 nanosheets encapsulated UiO-66 octahedral nanoparticles for visible-light-driven hydrogen generation, *Appl. Catal., B*, 2020, **260**, 118152.
- 46 N. Chang, D.-Y. He, Y.-X. Li, Z.-W. Tang and Y.-F. Huang, Fabrication of TiO_2 @MIL-53 core-shell composite for exceptionally enhanced adsorption and degradation of non-ionic organics, *RSC Adv.*, 2016, **6**, 71481–71484.
- 47 J.-D. Xiao, L. Han, J. Luo, S.-H. Yu and H.-L. Jiang, Integration of Plasmonic Effect and Schottky Junction into Metal–Organic Framework Composites: Steering Charge Flow for Enhanced Visible-Light Photocatalysis, *Angew. Chem., Int. Ed.*, 2017, **57**, 1103–1107.
- 48 S. Yan, S. Ouyang, H. Xu, M. Zhao, X. Zhang and J. Ye, Co-ZIF-9/ TiO_2 nanostructure for superior CO_2 photoreduction activity, *J. Mater. Chem. A*, 2016, **4**, 15126–15133.
- 49 H. Yi, D. Huang, L. Qin, G. Zeng, C. Lai, M. Cheng, S. Ye, B. Song, X. Ren and X. Guo, Selective prepared carbon nanomaterials for advanced photocatalytic application in environmental pollutant treatment and hydrogen production, *Appl. Catal., B*, 2018, **239**, 408–424.
- 50 Q. Hu, Y. Chen, M. Li, Y. Zhang and H. Li, Construction of NH_2 -UiO-66/ BiOBr composites with boosted photocatalytic activity for the removal of contaminants, *Colloids Surf., A*, 2019, **579**, 123625.
- 51 T. C. Nugent and M. El-Shazly, Chiral amine synthesis—recent developments and trends for enamide reduction, reductive amination, and imine reduction, *Adv. Synth. Catal.*, 2010, **352**, 753–819.
- 52 J.-H. Xie, S.-F. Zhu and Q.-L. Zhou, Transition Metal-Catalyzed Enantioselective Hydrogenation of Enamines and Imines, *Chem. Rev.*, 2011, **111**, 1713–1760.
- 53 X. Yang, S. Zhang, P. Li, S. Gao and R. Cao, Visible-light-driven photocatalytic selective organic oxidation reactions, *J. Mater. Chem. A*, 2020, **8**, 20897–20924.
- 54 L. Zeng, X. Guo, C. He and C. Duan, Metal–Organic Frameworks: Versatile Materials for Heterogeneous Photocatalysis, *ACS Catal.*, 2016, **6**, 7935–7947.
- 55 C. Xu, H. Liu, D. Li, J.-H. Su and H.-L. Jiang, Direct evidence of charge separation in a metal–organic framework:

- efficient and selective photocatalytic oxidative coupling of amines via charge and energy transfer, *Chem. Sci.*, 2018, **9**, 3152–3158.
- 56 D. Sun, L. Ye and Z. Li, Visible-light-assisted Aerobic Photocatalytic Oxidation of Amines to Imines over $\text{NH}_2\text{-MIL-125(Ti)}$, *Appl. Catal., B*, 2015, **164**, 428–432.
- 57 L. Zeng, T. Liu, C. He, D. Shi, F. Zhang and C. Duan, Organized aggregation makes insoluble perylene diimide efficient for the reduction of aryl halides *via* consecutive visible light-induced electron transfer processes, *J. Am. Chem. Soc.*, 2016, **138**, 3958–3961.
- 58 F.-J. Zhao, G. Zhang, Z. Ju, Y.-X. Tan and D. Yuan, The Combination of Charge and Energy Transfer Processes in MOFs for Efficient Photocatalytic Oxidative Coupling of Amines, *Inorg. Chem.*, 2020, **59**, 3297–3303.
- 59 P. Chen, Z. Guo, X. Liu, H. Lv, Y. Che, R. Bai, Y. Chi and H. Xing, A visible-light-responsive metal–organic framework for highly efficient and selective photocatalytic oxidation of amines and reduction of nitroaromatics, *J. Mater. Chem. A*, 2019, **7**, 27074–27080.
- 60 Y. Sha, J. Zhang, D. Tan, F. Zhang, X. Cheng, X. Tan, B. Zhang, B. Han, L. Zheng and J. Zhang, Hierarchically macro–meso–microporous metal–organic framework for photocatalytic oxidation, *Chem. Commun.*, 2020, **56**, 10754–10757.
- 61 H. Liu, Z. Guo, H. Lv, X. Liu, Y. Che, Y. Mei, R. Bai, Y. Chi and H. Xing, Visible-light-driven self-coupling and oxidative dehydrogenation of amines to imines via a Mn(II) -based coordination polymer, *Inorg. Chem. Front.*, 2020, **7**, 1016–1025.
- 62 J. Shi, J. Zhang, T. Liang, D. Tan, X. Tan, Q. Wan, X. Cheng, B. Zhang, B. Han, L. Liu and F. Zhang, Bipyridyl-Containing Cadmium–Organic Frameworks for Efficient Photocatalytic Oxidation of Benzylamine, *ACS Appl. Mater. Interfaces*, 2019, **11**, 30953–30958.
- 63 L. M. Aguirre-Díaz, N. Sneško, M. Iglesias, F. Sanchez, E. Gutierrez-Puebla and M. A. Monge, Efficient Rare-Earth-Based Coordination Polymers as Green Photocatalysts for the Synthesis of Imines at Room Temperature, *Inorg. Chem.*, 2018, **57**, 6883–6892.
- 64 H. Wei, Z. Guo, X. Liang, P. Chen, H. Liu and H. Xing, Selective Photooxidation of Amines and Sulfides Triggered by a Superoxide Radical Using a Novel Visible-Light-Responsive Metal–Organic Framework, *ACS Appl. Mater. Interfaces*, 2019, **11**, 3016–3023.
- 65 R. Liu, S. Meng, Y. Ma, L. Niu, S. He, X. Xu, B. Su, D. Lu, Z. Yang and Z. Lei, Atmospheric oxidative coupling of amines by UiO-66-NH_2 photocatalysis under milder reaction conditions, *Catal. Commun.*, 2019, **124**, 108–112.
- 66 T. Wang, X. Tao, Y. Xiao, G. Qiu, Y. Yang and B. Li, Charge separation and molecule activation promoted by Pd/MIL-125-NH_2 hybrid structures for selective oxidation reactions, *Catal. Sci. Technol.*, 2020, **10**, 138–146.
- 67 X. Yang, T. Huang, S. Gao and R. Cao, Boosting photocatalytic oxidative coupling of amines by a Ru-complex-sensitized metal–organic framework, *J. Catal.*, 2019, **378**, 248–255.
- 68 S. Zhang, K. Chen, W. Peng and J. Huang, $\text{g-C}_3\text{N}_4/\text{UiO-66-NH}_2$ nanocomposites with enhanced visible light photocatalytic activity for hydrogen evolution and oxidation of amines to imines, *New J. Chem.*, 2020, **44**, 3052–3061.
- 69 R. Wu, S. Wang, Y. Zhou, J. Long, F. Dong and W. Zhang, Chromium-Based Metal–Organic Framework MIL-101 Decorated with CdS Quantum Dots for the Photocatalytic Synthesis of Imines, *ACS Appl. Nano Mater.*, 2019, **2**, 6818–6827.
- 70 Y. Xiao, G. Tian, W. Li, Y. Xie, B. Jiang, C. Tian, D. Zhao and H. Fu, *J. Am. Chem. Soc.*, 2019, **141**, 2508–2515.